Chinese Chemical Letters 34 (2023) 107525

Contents lists available at ScienceDirect

Chinese Chemical Letters

journal homepage: www.elsevier.com/locate/cclet

An in-depth mechanistic insight into the redox reaction and degradation of aqueous Zn-MnO_2 batteries

Zongyuan You, Wei Hua, Na Li, Huanyan Liu, Jian-Gan Wang*

State Key Laboratory of Solidication Processing, Center for Nano Energy Materials, School of Materials Science and Engineering, Northwestern Polytechnical University, Shaanxi Joint Lab of Graphene (NPU), Xi'an 710072, China

ARTICLE INFO

Article history:
Received 19 April 2022
Revised 6 May 2022
Accepted 12 May 2022
Available online 16 May 2022

Keywords:
Zinc-ion battery
MnO_2 cathode
Working mechanism
Degradation mechanism
Zinc anode

ABSTRACT

Rechargeable aqueous Zn/MnO_2 batteries raise massive research activities in recent years. However, both the working principle and the degradation mechanism of this battery chemistry are still under debate. Herein, we provide an in-depth electrochemical and structural investigation on this controversial issue based on α-MnO_2 crystalline nanowires. Mechanistic analysis substantiates a two-electron reaction pathway of Mn^{2+}/Mn^{4+} redox couple from part of MnO_2 accompanying with a reversible precipitation/dissolution of flaky zinc sulfate hydroxide (ZSH) during the discharge/charge processes. The formation of the ZSH layer is double-edged, which passivates the deep dissolution of MnO_2 upon discharging, but promotes the electrochemical deposition kinetics of active MnO_2 upon charging. The cell degradation originates primarily from the corrosion failure of metallic zinc anode and the accumulation of irreversible $ZnMn_2O_4$ phases on the cathode. The addition of $MnSO_4$ to the electrolyte could afford supplementary capacity contribution *via* electro-oxidation of Mn^{2+}. However, a high $MnSO_4$ concentration will expedite the cell failure by corroding the metallic zinc anodes. The present study will shed a fundamental insight on developing new strategies toward practically viable Zn/MnO_2 batteries.

© 2023 Published by Elsevier B.V. on behalf of Chinese Chemical Society and Institute of Materia Medica, Chinese Academy of Medical Sciences.

Electrochemical energy storage technologies play an important role in updating the current energy infrastructure from clean and renewable power sources, such as solar and wind powers [1–3]. Among various energy storage candidates, rechargeable aqueous zinc-ion batteries (ZIBs) have received tremendous interest in scientific and technological communities owing to their advantages of high safety, low cost, eco-friendliness, and rich in natural resources [4–6]. Compared to the competing cathode materials of vandium-based compounds and prussian blue anologues, manganese oxides (*e.g.*, MnO_2) stand out in terms of both high operating voltage (~1.3 V *vs.* Zn^{2+}/Zn) and high specific capacity, making the Zn/MnO_2 battery chemistry particularly attractive [7–9].

In recent years, a vast number of studies have developed various strategies, including nanostructuring, doping or pre-intercalation with metal cations or water, defect engineering, and electrolyte formulation, to modify the performance of MnO_2 [5,10–12]. However, it is noted that the fundamental working mechanism of MnO_2 remains to be a controversial issue at present. Generally, four energy storage mechanisms have been proposed so far: (i) reversible (de)intercalation of Zn^{2+} [13–15], (ii) conversion reaction of H^+ [16], (iii) co-(de)intercalation of Zn^{2+} and H^+ [17–19], and (iv) electrolytic deposition/dissolution of MnO_2 [20–22]. The former three ones are on the basis of one-electron Mn^{3+}/Mn^{4+} reaction (theoretical capacity: 308 mAh/g), and the latter one is based on two-electron Mn^{2+}/Mn^{4+} reaction (theoretical capacity: 616 mAh/g). Literature survey of various MnO_2 cathodes indicates an initial specific capacity of <300 mAh/g, enabling the one-electron Mn^{3+}/Mn^{4+} reaction mechanism more reasonable and popular [23–26]. Nevertheless, a few studies found that the fully-discharged cathode is merely composed of the pristine MnO_2 phase structure [20–22], which completely contradicts the formation of MnOOH or $ZnMn_2O_4$ products based on one-electron reaction. It is also worth to mention that zinc sulfate hydroxide (ZSH) phase will be formed on the cathode surface upon discharging [27,28], which further complicates the discharged product identity. The ZSH is usually considered to be an undesirable by-product [16,29,30], the role of which, however, is still unclear during the charge/discharge processes. These discrepancies inspires us to present an in-depth understanding of the fundamental reaction mechanism and the associated ZSH issues.

It is well-documented that Jahn-Teller distortion of Mn^{3+} will inevitably generate highly soluble Mn^{2+} species *via* a notable disproportionation reaction (*i.e.*, $2Mn^{3+} \rightarrow Mn^{2+} + Mn^{4+}$), thus result-

* Corresponding author.
E-mail address: wangjiangan@nwpu.edu.cn (J.-G. Wang).

https://doi.org/10.1016/j.cclet.2022.05.039
1001-8417/© 2023 Published by Elsevier B.V. on behalf of Chinese Chemical Society and Institute of Materia Medica, Chinese Academy of Medical Sciences.

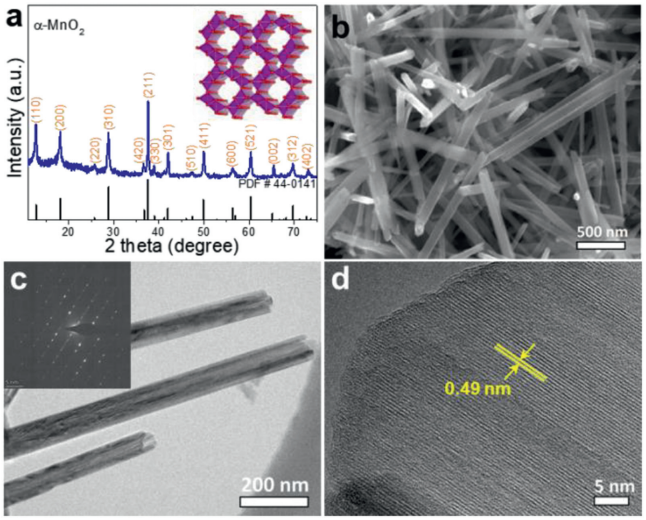

Fig. 1. (a) XRD pattern, (b) SEM, (c) TEM, SAED (inset) and (d) HRTEM images of MnO_2 sample.

ing in structural instability regardless of the pristine crystal structure of $\alpha/\beta/\delta/\gamma$-$MnO_2$ [23,31]. To mitigate the loss of active Mn from MnO_2, pre-addition of Mn^{2+} to the electrolyte with a proper concentration of 0.1–0.5 mol/L is regarded as the most promising way to date [16,32]. Outstanding lifetime beyond thousands of cycles have been achieved at a high current rate $\geq$ 1 A/g in many previous studies [16,26,33–35]. Despite of these achievements, the cycling performance of MnO_2 at a low current rate of 100 mA/g is still a formidable challenge [5,6]. Why the Mn^{2+} additive cannot solve the poor low-rate cycling problem? To answer this troublesome question, it is highly indispensable to unveil the role of Mn^{2+} and thus the capacity degradation mechanism.

Bearing this motivation in mind, the present work aims to provide an in-depth insight into the fundamental mechanisms of redox reaction and cell degradation through a systematic electrochemical and structural investigation on α-MnO_2 crystalline nanowires. It is revealed that our Zn-MnO_2 cell experiences a two-electron reaction mechanism accompanying with a reversible dissolution/deposition of MnO_2 and precipitation/dissolution of flaky ZSH layer during discharge/charge processes. The ZSH plays a double-edged role: (i) Serving as a passivation layer to inhibit deep dissolution of MnO_2 upon discharging, and (ii) promoting the electrochemical deposition kinetics of active MnO_2 upon charging. The addition of Mn^{2+} to the electrolyte could contribute supplementary capacity to maintain the cycling stability at high current densities, but a higher Mn^{2+} concentration (*e.g.*, 0.5 mol/L) will expedite the cell failure by corroding the metallic zinc anodes. Moreover, the corrosion of zinc anode and the accumulation of less reversible $ZnMn_2O_4$ phases on the cathode collectively result in the cell degradation.

MnO_2 materials were prepared by a simple hydrothermal method. Fig. 1 shows the physiochemical characterizations of the as-prepared sample. The sharp diffraction peaks in XRD pattern (Fig. 1a) can be readily assigned to the high-pure tetragonal α-MnO_2 phase with a typical [2 × 2] tunnel structure [36]. The structural information is further confirmed by Raman spectrum (Fig. S1 in Supporting information), in which the distinctive Raman bands at 583 and 641 cm^{-1} belong to the stretching symmetric Mn-O vibrations of [MnO_6] basic slabs while those at 184 and 389 cm^{-1} correspond to the deformation modes of Mn-O-Mn chains [18,37]. The SEM (Fig. 1b) observation indicates that the MnO_2 material is typical of one-dimensional nanowire morphology with smooth surface. TEM imaging (Fig. 1c) validates the straight nanowire feature having an average diameter of *ca.* 100 nm. The selected area electronic diffraction (SAED) of a single nanowire displays a set of well-defined pattern spots, indicating high-quality single crystalline characteristics of the α-MnO_2. The HRTEM (Fig. 1d) exhibits clear lattice fringes with a distance of 0.49 nm, agreeing well with the interplanar spacing of (200) planes. The MnO_2 nanowires possess a BET specific surface area of 17.9 m^2/g (Fig. S2 in Supporting information). The surface chemistry of the sample was examined by XPS technique. As shown in Fig. S3a (Supporting information), the survey spectrum reveals the presence of Mn, O and K elements. The K presence can be attributed to the incorporation of K^+ cations into the [2 × 2] tunnels for stabilizing the α-MnO_2 structure. The high resolution Mn 2p spectrum (Fig. S3b in Supporting information) displays Mn $2p_{1/2}$ and Mn $2p_{3/2}$ peaks at 654.7 and 642.9 eV, respectively, corresponding to a typical spin energy gap of 11.8 eV for MnO_2 [25]. The core-level O 1s spectrum (Fig. S3c in Supporting information) can be fitted by two species of tetravalent Mn-O-Mn component at 530 eV and hydrated trivalent Mn-OH component at 531.4 eV. According to the envelope proportion of Mn-O-Mn and Mn-OH components [38,39], the average Mn valence of MnO_2 calculated to be +3.81, which is in good accordance with the value determined by the Mn 3s spectrum (Fig. S3d in Supporting information).

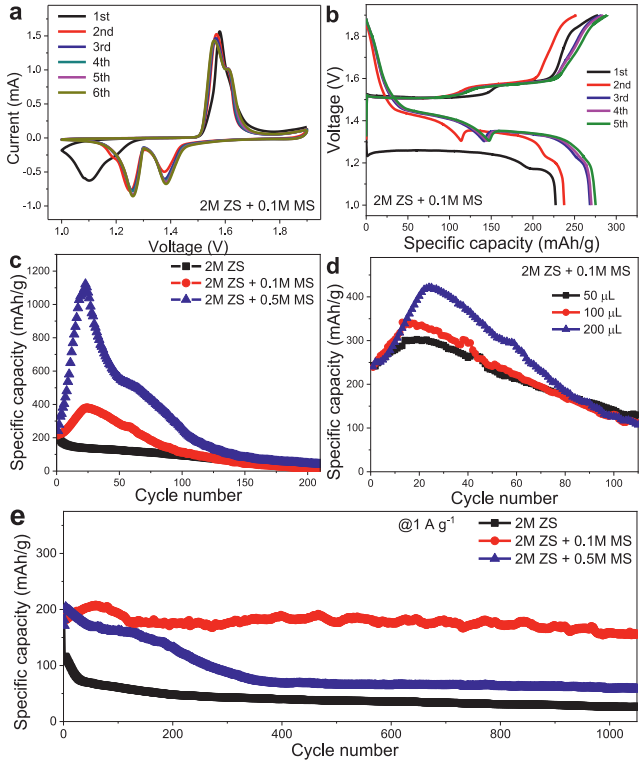

Fig. 2. (a) CV curves, (b) galvanostatic charge/discharge profiles of MnO_2 cathodes in 2 mol/L $ZnSO_4$ + 0.1 mol/L $MnSO_4$ electrolyte. Cycling performance of cells at a current rate of (c) 0.1 A/g and (e) 1 A/g (200 μL electrolyte). (d) Effect of electrolyte amount on the specific capacity.

The as-prepared α-MnO_2 materials were employed as the cathodes of ZIBs to evaluate their electrochemical properties in three different aqueous electrolytes of 2 mol/L $ZnSO_4$ (2 M ZS), 2 mol/L $ZnSO_4$ + 0.1 mol/L $MnSO_4$ (2 M ZS + 0.1 M MS) and 2 mol/L $ZnSO_4$ + 0.5 mol/L $MnSO_4$ (2 M ZS + 0.5 M MS). Fig. 2a, Figs. S4 and S5 (Supporting information) show the initial six CV curves. It is noted that the α-MnO_2 cathodes share an identical CV shape in the three electrolytes, indicating the same reaction chemistry. The electrochemical behavior is further confirmed by the galvanostatic

charge/discharge profiles (Fig. 2b), in which the stepwise voltage plateaus are in close association with the insertion of H^+ and/or Zn^{2+}. However, there is no consensus on the detailed working mechanism of MnO_2 at present. A number of previous studies evidenced that the discharge process is a one-electron solid/solid reaction (Mn^{4+}(s) ↔ Mn^{3+}(s), *e.g.*, MnOOH and $ZnMn_2O_4$ as the products) [16,17]. Some recent research substantiated a purely two-electron solid-liquid reaction mechanism (Mn^{4+}(s) ↔ Mn^{2+}(l)) [20,22]. Hence, it is highly indispensable to unveil the true mechanism, which will be specified in the following section.

Fig. 2c exhibits the cycling performance of the ZIB cells at 0.1 A/g in different electrolytes. The specific capacity of the cell shows a continuous decrease in pure $ZnSO_4$ electrolyte, which can be ascribed to the structural instability caused by the John-Teller effect of Mn^{3+} that produces soluble Mn^{2+} *via* disproportionation reaction [21]. The addition of Mn^{2+} in the electrolyte is generally considered to be a feasible approach to stabilize the MnO_2 structure by suppressing the disproportionation reaction of Mn^{3+} [16,40,41]. However, in the electrolytes containing different $MnSO_4$ concentrations, it is interesting to notice that both cells show a sharp increase of the capacity in the initial 30 cycles and then a fast capacity degradation. In particular, the cell delivers an incredible specific capacity of 1240 mAh/g in 2 M ZS + 0.5 M MS, which is double of the theoretical value even based on two-electron reaction (616 mAh/g). This suggests that the capacity calculation based on the initial MnO_2 mass is absolutely inappropriate in electrolytes containing $MnSO_4$ additive, making the performance comparison unfair among different studies. The capacity gain is related to the electro-oxidation of Mn^{2+} into new active MnO_2 species, as confirmed by the short charging voltage plateau at >1.8 V (Fig. 2b) and the increasing capacity for the carbon black electrode (Fig. S6 in Supporting information). The phenomenon indicates that the Mn^{2+} amount in the electrolyte makes a critical contribution to the total capacity. In addition to the $MnSO_4$ concentration, it is believed that the electrolyte volume is also an important parameter for the capacity delivery. As evidenced in Fig. 2d and Fig. S7 (Supporting information), the capacity summit increases with the increasing usage of the electrolyte volume. Therefore, for the Zn-MnO_2 battery system, it is necessary to point out the Mn^{2+} concentration, the electrolyte volume, and the MnO_2 loading in one cell to enable a meaningful electrochemical evaluation of the materials and a fair comparison with the documented literature [42].

The galvanostatic charge/discharge profiles of the cell at different current densities in 2 M ZS + 0.1 M MS are displayed in Fig. S8 (Supporting information). At a high current rate of 2 A/g, the cell could deliver a higher capacity of 138 mAh/g in the electrolytes containing $MnSO_4$ than that in ZS electrolyte. In addition, the two-stage discharge plateau is clearly visible at lower current rates (<0.5 A/g) and the contribution ration of the upper discharge plateau increases from 55.8% to 80.2% as the current rate rises from 0.1 A/g to 2 A/g (Fig. S9 in Supporting information), indicating that the lower discharge plateau is a kinetically-limited reaction. The capacity contribution from the two plateaus during the cycling test is further quantified in Fig. S10 (Supporting information). Notably, the contribution from the upper discharge plateau is increasing from 50% to 73% after 150 cycles, suggesting that the upper discharge process is more reversible than the lower counterpart. Since the less reversible lower discharge plateau could be suppressed at high current rates, it is expected that the cycling performance can be greatly improved at a high current rate of 1.0 A/g. As shown in Fig. 2e, the cell manifests excellent cycling performance in 2 M ZS + 0.1 M MS over 1100 cycles. That's the reason why many previous-reported studies could obtain outstanding cycling performance at high current densities. Herein, it should be noted that the cycling performance in 2 M ZS + 0.5 M MS is much poorer than that in 2 M ZS + 0.1 M MS. We ascribe it to the metallic Zn anode problem, which will be clarified in the subsequent degradation discussion.

Ex situ XRD, SEM and TEM techniques were carried out to probe the intrinsic mechanism of MnO_2 by investigating the structural and morphological evolution during the first two cycles. When the cell is fully discharged to 1.0 V (point B in Fig. 3a), the peak intensity of α–MnO_2 weakens significantly, and the new set of diffraction peaks can be assigned to hydrated zinc sulfate hydroxide (ZSH, $Zn(OH)_2SO_4{\cdot}5H_2O$) phase (Fig. 3b) [21,32]. A thick layer of ZSH flakes is precipitated on the cathode surface (Fig. 3d and Fig. S11 in Supporting information), compared to the pristine nanowire morphology (Fig. 3c). The formation of ZSH phase is further confirmed by the homogeneous distribution of Zn, S and O elements throughout the flake (Fig. S12 in Supporting information). It should be mentioned that the complex diffraction peaks of ZSH phase are almost overlapping with that of MnOOH and $ZnMn_2O_4$, which usually conclude misleading information. For example, some weak diffraction peaks are usually identified as MnOOH (*e.g.*, the peak at *ca.* 21°) or $ZnMn_2O_4$ (*e.g.*, the peaks at *ca.* 32°−36°) in previous studies [13,17]. TEM imaging is then conducted to clarify this discrepancy, and the result reveals that the fully-discharged sample is merely composed of single-crystalline α–MnO_2 nanowires (Figs. 3e and f). However, there are many dissolved areas in the nanowire body from the dark-field TEM image (Fig. S13 in Supporting information), indicating the discharge process is a dissolution process (*i.e.*, $MnO_2 \rightarrow Mn^{2+}$). To further validate it, the ZSH layer was washed by diluted acetate acid. It is observed that only α–MnO_2 nanowires are present in the washed cathode (Fig. S14 in Supporting information).

After fully charged (point C), the cathode recovers the α–MnO_2 phase yet with much weaker diffraction intensity (Fig. 3b). The ZSH flakes are dissolved from the cathode surface and the nanowires are restored as observed from the SEM image (Fig. 3g). Interestingly, the nanowire surface is covered by a layer of nanoporous nanosheets, the phase of which cannot be detected by the XRD technique. The unique core-sheath nanowire/nanosheet architecture is clearly visible by TEM imaging (Fig. 3h). The corresponding SAED analysis shows two sets of diffraction patterns, in which the disperse rings belong to the low-crystalline birnessite-type δ-MnO_2. The lattice spacing of 0.69 nm in the HRTEM (Fig. 3i) corresponds to the (002) planes of birnessite-type δ-MnO_2, revealing that the charging process is an electro-oxidation of Mn^{2+} into birnessite-type δ-MnO_2 accompanying with the ZSH dissolution. The discharging process in the second and following cycles involves a two-stage reaction. As displayed in Figs. 3j and k, the cathode maintains the hybrid morphology of nanowire/nanosheet after the upper discharge plateau (point D). In addition, a small amount of ZSH nanoflakes start to precipitate on the surface. The EDX elemental analysis of the nanosheets illustrates a higher Zn content of 13.63% (area 2, Fig. 3l) compared to the naked nanowire (area 1, 0.54%), indicating that the birnessite-type δ-MnO_2 is more energetically favorable for the insertion of Zn^{2+} ions than the α–MnO_2. A deeper discharging to 1.0 V (point E) results in the growth of microsized ZSH flakes and the dissolution of the outer MnO_2 nanosheets (Fig. S15 in Supporting information). And the subsequent re-charging process achieves the re-generation of nanowire/nanosheet morphology and the removal of ZSH flakes (Fig. S16 in Supporting information), indicating a highly reversible reaction.

The above mechanistic discussion herein substantiates a two-electron solid-liquid MnO_2/Mn^{2+} reaction pathway accompanying with a reversible precipitation/dissolution of a ZSH layer. However, it is noted that the initial specific capacity of MnO_2 is much lower than the theoretical value based on the two-electron reaction, indicating that part of MnO_2 (~45%) participates in the discharge process. The reason can be attributed to the formation of

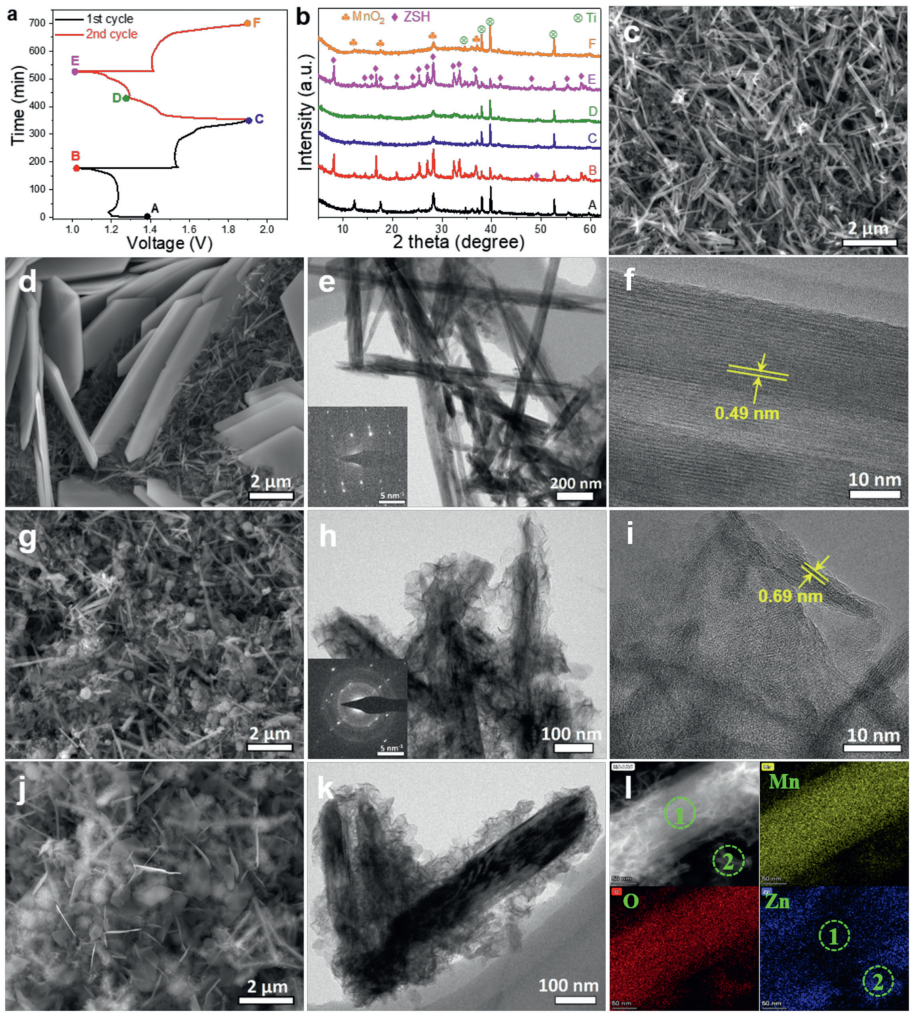

Fig. 3. (a) The initial two charge/discharge profiles, (b) *ex-situ* XRD patterns of the MnO_2 cathodes collected from different states. SEM, TEM, SAED (inset), HRTEM, and EDX elemental mapping images of the cathodes at (c) pristine A state, (d–f) fully-discharged B state, (g–i) fully-charged C state, and (j–l) partially-discharged D state.

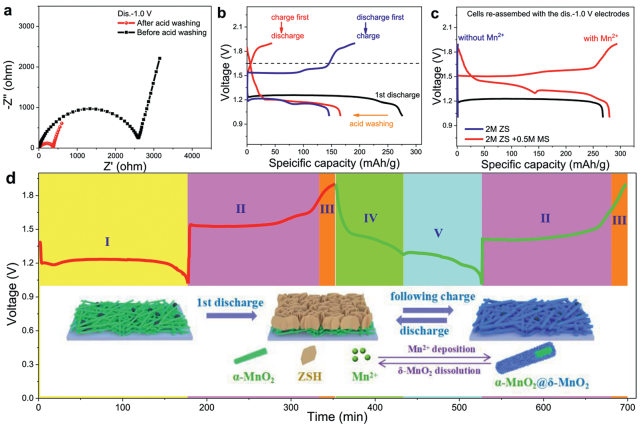

Fig. 4. (a) EIS spectra of the fully-discharged cathodes before and after acid washing. (b) Charge/discharge curves of the cells re-assembled with the acid-washed cathodes at 0.05 A/g. (c) Charge/discharge curves of the cells re-assembled with the discharged cathodes without acid washing. (d) Schematic illustration of working mechanism of α-MnO_2 cathodes.

the thick ZSH inert layer covered on the electrode surface, which passivates the deep reduction dissolution of MnO_2. This is proved by the EIS (Fig. 4a), from which the charge-transfer resistance (R_{ct}) of the fully-discharged cell is measured to be as high as 2610 Ω. When the ZSH layer is removed, the R_{ct} of the re-assembled cell (electrolyte: 2 M ZS + 0.1 M MS) is remarkably reduced to 405 Ω. More importantly, the re-assembled cell could deliver a discharge capacity of 147 mAh/g based on the initial MnO_2 mass (Fig. 4b), corresponding to 267 mAh/g based on the remnant MnO_2 mass. The result validates the passivation role of the ZSH layer on impeding further discharge of MnO_2. In addition, if the re-assembled cell is charged at first, the charge plateau in the voltage range of 1.5–1.6 V disappears, and a higher potential (>1.8 V) is required to drive the oxidation of Mn^{2+} in the absence of ZSH, suggesting that the ZSH layer is of critical benefit for the electro-deposition of MnO_2. To further discuss the MnO_2/Mn^{2+} reaction, the fully-discharged cathodes were taken out to re-assemble new cells using fresh electrolytes with and without $MnSO_4$ additive. As shown in Fig. 4c, the cell cannot operate in the electrolyte without Mn^{2+}. By contrast, normal charge/discharge profiles are obtained in the electrolyte containing Mn^{2+}, confirming the dissolution/deposition mechanism. Moreover, the direct oxidation of Mn^{2+} in the absence of ZSH is also proved by the cell using carbon black (CB) as the cathode in the electrolyte containing $MnSO_4$ (Fig. S6). It is worth pointing out that the oxidation of Mn^{2+} is a kinetically sluggish process. As shown in Fig. S6b, the CB-cell exhibits increasing specific capacity at a low current rate of 0.1 mA/cm^2, but negligible

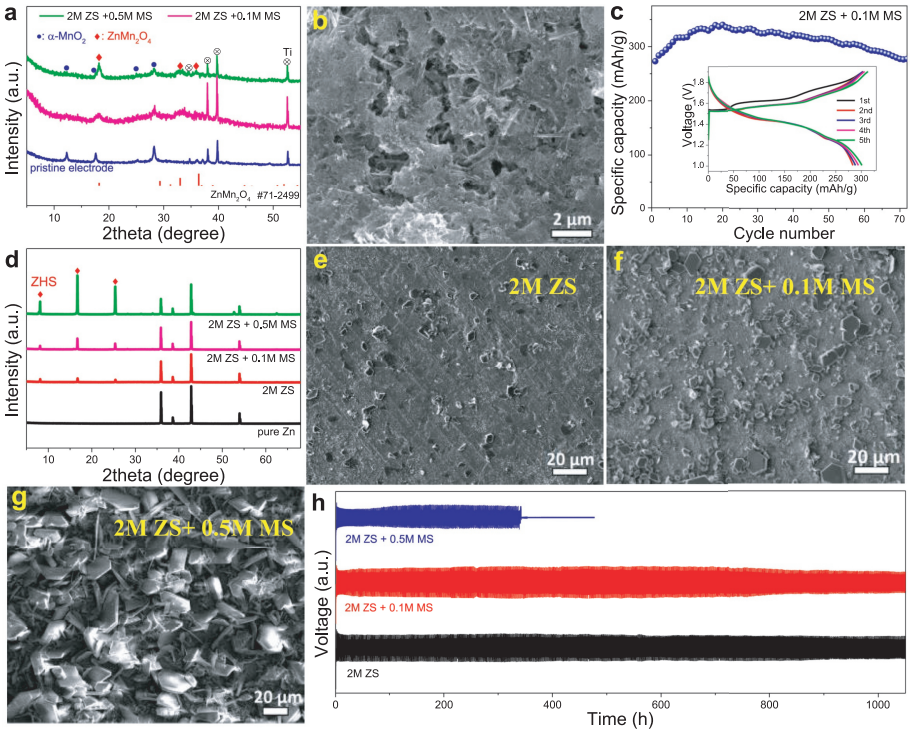

Fig. 5. (a) XRD pattern and (b) SEM image of the MnO_2 cathodes after the cycling test at 0.1 A/g. (c) Cycling performance of the cycled MnO_2 cathode re-assembled with a fresh Zn anode, and the inset shows the corresponding charge/discharge curves. (d) XRD of the Zn anodes in different electrolytes. (e–g) SEM images of the Zn anodes after soaking in different electrolytes for 10 days. (h) Long-term cycling stability of the Zn/Zn symmetric cells in different electrolytes.

capacity at a high current rate of 1 mA/cm^2, agreeing well with the earlier result in Fig. 2c.

Based on the in-depth structural and electrochemical analysis, Fig. 4d illustrates the working mechanism of Zn/MnO_2 battery. The first discharge/charge stages I/II in Fig. 4d indicate a partial dissolution process of α-MnO_2, which can be written as [20]:

$$3MnO_2 + 8Zn^{2+} + 2SO_4^{2-} + 16H_2O + 6e^- \leftrightarrow 3Mn^{2+} + 2Zn_4SO_4(OH)_6{\cdot}5H_2O\downarrow \quad (1)$$

The ZSH phase is usually regarded as undesirable by-products [43]. Nevertheless, the formation of ZSH phase is double-edged, which not only functions as a passivation layer to impede deep dissolution of MnO_2 upon discharging, but also promotes the electrodeposition kinetics of birnessite-type MnO_2 upon charging. Additionally, the $MnSO_4$ additive in the electrolyte can be electrochemically oxidized into new active species at a higher potential of >1.8 V (stage III, *i.e.*, $Mn^{2+} + 2H_2O \rightarrow MnO_2 + 4H^+$), thereby making an extra contribution to the total capacity.

In the following discharge/charge cycles, the as-deposited birnessite-type δ-MnO_2 could provide large layered channels for insertion of Zn^{2+}/H^+ with a smaller overpotental (stage IV):

$$MnO_2 + x\ Zn^{2+}/H^+ + xe^- \leftrightarrow (Zn/H)xMnO_2 \quad (2)$$

The subsequent lower discharge plateau (stage V) is similar to the Eq. 1, which is a typical dissolution of (Zn/H)$x$$MnO_2$ along with a simultaneous precipitation of ZSH flakes.

As discussed in Fig. 2c, regardless of the electrolyte containing $MnSO_4$ or not, the ZIB cells can retain no more than 20 mAh/g after 200 cycles at a low current density of 0.1 A/g. The previous studies generally ascribe the poor cycling performance of MnO_2 to its structural instability caused by Jehn-teller effect [16,21]. To this end, a great number of design strategies, such as pre-intercalation/doping of metal ions (*e.g.*, K^+, Zn^{2+}, Ca^{2+}, Co^{2+}) and surface coating, have been proposed to stabilize the MnO_2 crystal framework [26,33,37,44–46]. Although improved cycle life was obtained, these achievements are usually based on the tests at high current densities (≥1 A/g). Scarcely do these studies present the cycling performance measured at <0.3 A/g beyond 100 cycles. In fact, from the perspective of the dissolution/deposition mechanism, it is meaningless to stabilize the MnO_2 matrix as the MnO_2 will inevitably suffer from structure reconstruction at each cycle. Hence, it is necessary to unveil the intrinsic degradation nature of the Zn/MnO_2 battery system.

Fig. 5a shows the XRD pattern of the cycled MnO_2 cathodes. The peak intensity of α-MnO_2 is greatly decreased primarily due to the partial dissolution of pristine α-MnO_2 upon discharging and the surface deposition of amorphous birnessite-type MnO_2 upon charging. The SEM image (Fig. 5b and Fig. S17 in Supporting information) confirms the formation of an amorphous layer and some underneath α-MnO_2 nanowires can still be observed. In addition to the α-MnO_2, there are some strong peaks that can be assigned to the $ZnMn_2O_4$ phase. Compared to MnO_2, $ZnMn_2O_4$ phase has been reported to be less electrochemically acive for ZIBs [47,48]. Guo *et al.* considered the main reason of capacity degradation as the formation of $ZnMn_2O_4$ [20]. However, in our work, when the cycled MnO_2 is re-assembled with a fresh Zn anode, the new cell could deliver a high and stable specific capacity of ~300 mAh/g at 0.1 A/g (Fig. 5c). Consequently, we believe that the capacity degradation is also in close relation to the Zn anode.

XRD analysis of the cycled Zn anodes reveals the formation of the ZSH phase (Fig. 5d). Notably, the peak intensity of the ZSH increases with the increasing concentration of $MnSO_4$, suggesting that the $MnSO_4$ additive exacerbates the corrosion problem of Zn anode. Fig. S18 (Supporting information) shows the optical photos of the cycled Zn anodes. It is observed that the Zn plate suffers from more severe corrosion issue in the electrolyte of 2 M ZS + 0.5 M MS than that in 2 M ZS + 0.1 M MS. To further probe

the chemical stability of Zn anodes, pure Zn plates were soaked in three different electrolytes for 10 days. The significant color change of the three Zn plates indicates a serious corrosion reaction (Fig. S19 in Supporting information). XRD identifies the formation of ZSH by-products, the peak intensity of which exhibits a similar increasing trend to the cycled anodes. The morphology of the Zn surface is compared by SEM imaging. Microsized ZSH particles are sparsely covered on the Zn surface after soaking in pure 2 M ZS electrolyte (Fig. 5e). The addition of $MnSO_4$ obviously aggravates the precipitation of ZSH particles (Figs. 5f and g). Remarkably, a high concentration of 0.5 mol/L $MnSO_4$ incurs a dense and thick ZSH flakes (Fig. 5g), validating the adverse role of the $MnSO_4$ additive on the stability of metallic Zn. Zn/Zn symmetric cells were assembled using the three different electrolytes to evaluate the long-term galvanostatic cycling stability at 1 mA/cm^2 (Fig. 5h). The cells show similar charge/discharge voltage profiles (Fig. S20 in Supporting information). The cells using both 2 M ZS and 2 M ZS + 0.1 M MS could maintain excellent cycling durability for more than 1050 h. In sharp contrast, the cell based on 2 M ZS + 0.5 M MS experiences inferior cycle life with a sudden reduction of the polarization voltage after 340 h. The cell decay is attributed to the dendrite-induced short circuit and accumulation of detrimental by-products [49–52]. As such, the worse cycling performance of the Zn/MnO_2 full cell in 2 M ZS + 0.5 M MS at the high current rate of 1 A/g (Fig. 2e) can be well rationalized by the poor electrochemical stability of Zn anode.

In summary, the fundamental mechanisms of redox reaction and degradation based on aqueous Zn/α-MnO_2 battery system is unveiled by an in-depth electrochemical and structural analysis. The working mechanism involves a two-electron solid-liquid redox reaction of MnO_2/Mn^{2+} from part of MnO_2 along with a concomitant precipitation/dissolution of a flaky ZSH layer during discharge/charge processes. The ZSH by-product is double-edged, forming a passivation layer to inhibit deep dissolution of MnO_2 upon discharging, but kinetically promoting the reversible deposition of MnO_2 upon charging. The capacity degradation is primarily ascribed to the anode failure induced by metallic zinc corrosion and the accumulation of irreversible $ZnMn_2O_4$ phases on the cathode. The employment of electrolytic $MnSO_4$ additive can contribute additional capacity to the total capacity by electrooxidation of Mn^{2+}, but cannot solve the cycling problem at a low current density (*e.g.*, 0.1 A/g). A high $MnSO_4$ concentration (*e.g.*, 0.5 mol/L) greatly exacerbates the corrosion of the metallic zinc anode, thereby downgrading the cycling stability of full cells. Moreover, to enable a fair and meaningful performance comparison, the critical cell parameters of Mn^{2+} concentration, electrolyte amount, and the initial MnO_2 loading, should be provided as a protocol for evaluating Mn-based materials. It is believed that the fundamental study will shed light on the development of novel strategies toward a practically viable Zn/MnO_2 battery technology.

Declaration of competing interest

The authors declare that they have no known competing financial interests or personal relationships that could have appeared to influence the work reported in this paper.

Acknowledgments

The authors would like to acknowledge the research fund of National Natural Science Foundation of China (No. 51821091), and Fundamental Research Funds for the Central Universities (Nos. D5000210894 and 3102019JC005). The authors also thank the support from the Analytical & Testing Center of Northwestern Polytechnical University for TEM analysis.

Supplementary materials

Supplementary material associated with this article can be found, in the online version, at doi:10.1016/j.cclet.2022.05.039.

References

[1] B. Dunn, H. Kamath, J.M. Tarascon, Science 334 (2011) 928–935.
[2] Z. Yang, J. Zhang, M. Kintner-Meyer, et al., Chem. Rev. 111 (2011) 3577–3613.
[3] S. Chu, Y. Cui, N. Liu, Nat. Mater. 16 (2016) 16–22.
[4] J. Ming, J. Guo, C. Xia, et al., Mater. Sci. Eng. R 135 (2019) 58–84.
[5] H. Liu, J.G. Wang, Z. You, et al., Mater. Today 42 (2021) 73–98.
[6] L.E. Blanc, D. Kundu, L.F. Nazar, Joule 4 (2020) 771–799.
[7] M. Song, H. Tan, D. Chao, et al., Adv. Funct. Mater. 28 (2018) 1802564.
[8] A. Konarov, N. Voronina, J.H. Jo, et al., ACS Energy Lett. 3 (2018) 2620–2640.
[9] B. Tang, L. Shan, S. Liang, et al., Energy Environ. Sci. 12 (2019) 3288–3304.
[10] X. Jia, C. Liu, Z.G. Neale, et al., Chem. Rev. 120 (2020) 7795–7866.
[11] K.W. Nam, H. Kim, J.H. Choic, et al., Energy Environ. Sci. 12 (2019) 1999–2009.
[12] L. Su, L. Liu, Y. Wang, et al., Chin. Chem. Lett. 31 (2020) 2358–2364.
[13] C. Xu, B. Li, H. Du, et al., Angew. Chem. Int. Ed. 51 (2012) 933–935.
[14] M.H. Alfaruqi, V. Mathew, J. Gim, et al., Chem. Mater. 27 (2015) 3609–3620.
[15] Z. Hou, M. Dong, Y. Xiong, et al., Small (2020) 2001228.
[16] H. Pan, Y. Shao, P. Yan, et al., Nat. Energy 1 (2016) 16039.
[17] W. Sun, F. Wang, S. Hou, et al., J. Am. Chem. Soc. 139 (2017) 9775–9778.
[18] J. Wang, J.G. Wang, H. Liu, et al., Adv. Funct. Mater. 31 (2020) 2007397.
[19] X.Z. Zhai, J. Qu, J. Wang, et al., Energy Storage Mater. 42 (2021) 753–763.
[20] X. Guo, J. Zhou, C. Bai, et al., Mater. Today Energy 16 (2020) 100396.
[21] B. Lee, H.R. Seo, H.R. Lee, et al., ChemSusChem 9 (2016) 2948–2956.
[22] J. Yang, J. Cao, Y. Peng, et al., ChemSusChem 13 (2020) 4103.
[23] N. Zhang, F. Cheng, J. Liu, et al., Nat. Commun. 8 (2017) 405–415.
[24] S. Lian, C. Sun, W. Xu, et al., Nano Energy 62 (2019) 79–84.
[25] D. Wang, L. Wang, G. Liang, et al., ACS Nano 13 (2019) 10643–10652.
[26] G. Fang, C. Zhu, M. Chen, et al., Adv. Funct. Mater. 29 (2019) 1808375.
[27] J. Huang, Z. Wang, M. Hou, et al., Nat. Commun. 9 (2018) 2906.
[28] J. Wang, J.G. Wang, X. Qin, et al., ACS Appl. Mater. Interfaces 12 (2020) 34949–34958.
[29] T. Zhang, Y. Tang, G. Fang, et al., Adv. Funct. Mater. (2020) 2002711.
[30] S. Zhao, B. Han, D. Zhang, et al., J. Mater. Chem. A 6 (2018) 5733–5739.
[31] B. Lee, H.R. Lee, H. Kim, et al., Chem. Commun. 51 (2015) 9265–9268.
[32] J. Wang, J.G. Wang, H. Liu, et al., J. Mater. Chem. A 7 (2019) 13727–13735.
[33] X. Zhu, Z. Cao, W. Wang, et al., ACS Nano 15 (2021) 2971–2983.
[34] X.Z. Zhai, J. Qu, S.M. Hao, et al., Nano Micro Lett. 12 (2020) 56.
[35] T. Sun, Q. Nian, S. Zheng, et al., Small 16 (2020) 2000597.
[36] M.H. Alfaruqi, J. Gim, S. Kim, et al., J. Power Sources 288 (2015) 320–327.
[37] Y. Zeng, X. Zhang, Y. Meng, et al., Adv. Mater. 29 (2017) 1700274.
[38] M. Toupin, T. Brousse, D. Bélanger, Chem. Mater. 16 (2004) 3184–3190.
[39] Y. Hou, Y. Cheng, T. Hobson, et al., Nano Lett. 10 (2010) 2727–2733.
[40] G. Fang, J. Zhou, A. Pan, et al., ACS Energy Lett. 3 (2018) 2480–2501.
[41] Y. Huang, J. Mou, W. Liu, et al., Nano Micro Lett. 11 (2019) 49–56.
[42] Y. Zhong, X. Xu, J. Veder, et al., iScience 23 (2020) 100943.
[43] S.H. Kim, S.M. Oh, J. Power Sources 72 (1998) 150–158.
[44] Q. Chen, J. Jin, Z. Kou, et al., Small 16 (2020) 2000091.
[45] F. Kataoka, T. Ishida, K. Nagita, et al., ACS Appl. Energy Mater. 3 (2020) 4720–4726.
[46] J. Huang, X. Tang, K. Liu, et al., Mater. Today Energy 17 (2020) 100475.
[47] X. Gao, H. Wu, W. Li, et al., Small 16 (2020) 1905842.
[48] S.D. Han, S. Kim, D. Li, et al., Chem. Mater. 29 (2017) 4874–4884.
[49] L. Ma, M.A. Schroeder, O. Borodin, et al., Nat. Energy 5 (2020) 743–749.
[50] X. Han, H. Leng, Y. Qi, et al., Chem. Eng. J. 431 (2022) 133931.
[51] J. Hao, B. Li, X. Li, et al., Adv. Mater. (2020) 2003021.
[52] L. Wang, G. Fan, J. Liu, et al., Chin. Chem. Lett. 32 (2021) 1095–1110.